RESEARCH ARTICLE

Fourier-Limited Attosecond Pulse from High Harmonic Generation Assisted by Ultrafast Magnetic Fields

Rodrigo Martín-Hernández[1]*, Hongtao Hu[2], Andrius Baltuska[2], Luis Plaja[1], and Carlos Hernández-García[1]

[1]Grupo de Investigación en Aplicaciones del Láser y Fotónica, Departamento de Física Aplicada, Universidad de Salamanca, E-37008 Salamanca, Spain. [2]Photonics Institute, Technische Universität Wien, A-1040 Vienna, Austria.

*Address correspondence to: rodrigomh@usal.es

One of the main constraints for reducing the temporal duration of attosecond pulses is the attochirp inherent to the process of high-order harmonic generation (HHG). Though the attochirp can be compensated in the extreme-ultraviolet using dispersive materials, this is unfeasible toward x-rays, where the shortest attosecond or even sub-attosecond pulses could be obtained. We theoretically demonstrate that HHG driven by a circularly polarized infrared pulse while assisted by an strong oscillating ultrafast intense magnetic field enables the generation of few-cycle Fourier-limited few attosecond pulses. In such a novel scenario, the magnetic field transversally confines the ionized electron during the HHG process, analogously to a nanowire trapping. Once the electron is ionized, the transverse electron dynamics is excited by the magnetic field, acting as a high-energy reservoir to be released in the form of phase-locked spectrally wide high-frequency harmonic radiation during the electron recollision with the parent ion. In addition, the transverse breathing dynamics of the electron wavepacket, introduced by the magnetic trapping, strongly modulates the recollision efficiency of the electronic trajectories, thus the attosecond pulse emissions. The aftermath is the possibility of producing high-frequency (hundreds of eV) attosecond isolated few-cycle pulses, almost Fourier limited. The isolated intense magnetic fields considered in our simulations, of tens of kT, can be produced in finite spatial volumes considering structured beams or stationary configurations of counter-propagating state-of-the-art multi-terawatt/petawatt lasers.

Introduction

Attosecond (*as*) pulses stand as one of the most robust tools to probe ultrafast electronic processes in matter [1–3]. The extension of pump-probe experiments to this timescale allows for time-resolved observation of electronic excitations [4,5]. They are also considered a main tool to understand, and ultimately control, charge migration in molecular systems [6], with huge implications for understanding the alteration of biological macromolecules [7], the development of more efficient photovoltaic systems [8], or more selective catalysts [9]. Though recent advances point to the full control of the generation of intense *as* pulses in free electron lasers [10,11], high-order harmonic generation (HHG) in gases stands as the most robust and coherent *as* source since their first generation in 2001 [4,12].

The origin of such success lies in the extreme coherence of HHG, which can be well understood by the semiclassical 3-step model [13]. When an intense infrared (IR) laser field interacts with a gas target, an electronic wavepacket is released from each atom or molecule. During its excursion through the continuum, the detached electrons quiver synchronized with the field oscillations, acquiring kinetic energy. Upon recollision with

the parent atoms, high-frequency harmonics are radiated, extending from the extreme-ultraviolet (EUV) toward the soft x-rays [14]. Two families of semiclassical electron paths—the so-called short and long trajectories according to their excursion time [15]—contribute to the harmonic emission. Since the trajectories are ordered in time, depending on the instant of ionization, high-order harmonics are emitted at different times and, therefore, with chirp—positive (negative) for the short (long) trajectories. As a result, the higher-order harmonics can be synthesized into *as* pulses, whose chirp—known as attochirp [16,17]—limits their pulse duration. Indeed, the broadest HHG spectrum reported to date, extending from the EUV to 1.6 keV, though being able to support 2.5-*as* Fourier-limited pulses, was estimated to be emitted as a 3-order-of-magnitude longer pulse (1.2 fs) due to the attochirp [14].

In the macroscopic picture, the attochirp from the electronic trajectories is translated from the microscopic picture through the coherent addition of the HHG emission from the emitters in the target. Depending on phase-matching conditions, short or long trajectory contributions will prevail, though the first ones are typically more robust under harmonic propagation [14,16]. The positive attochirp of short trajectory contributions

(which are the most robust under macroscopic phase-matching [18]) can be compensated through the use of negative dispersive materials. For example, López-Martens et al. [19] combined a 600-nm-thick Al film with spatial filtering to reach almost Fourier-transform-limited single-cycle 170-*as* pulses from a 0.8-µm driver field; Li et al. [20] used a 400-nm tin filter to reach 53-*as* pulses from two 1.8-µm driver fields; and Gaumnitz et al. [21] used a 100-nm-thick Zr filter to report the shortest attosecond pulse to date, 43 *as*, driven by a 1.8-µm laser field. However, such compensation is very limited when approaching the x-rays, where the use of dispersive materials is impractical. As a consequence, though HHG stands as the most robust tool to generate coherent spectra toward the soft x-rays, specially with the use of mid-IR drivers [14,22–24], the generation of shorter *as* pulses is strongly limited by their attochirp. As an alternative, several approaches have been considered modifying the HHG trajectories—and thus the high-order harmonic properties, including the attochirp—by shaping the driving field. Among them are the use of multicolor drivings [25,26], the use of complex polarization schemes [27,28], the non-homogeneity of the field amplitude [29], the non-adiabaticity resulting from very intense laser fields [30], and the inclusion of static electric fields (E-fields) [31] or magnetic fields (B-fields). Indeed, up to now, the consideration of B-fields in the process of HHG has been limited to point out the relevance of relativistic effects when using mid-IR drivers [32,33] or the use of static fields [34,35]. In the latter case, it was found that the transverse electronic spread during the continuum travel could be controlled, leading to more efficient emission for some harmonic orders when the ionized electron wavepacket rescattered back against the parent ion in times multiple of the cyclotron period.

As we demonstrate in this article, the recent development of structured ultrahigh-power ultrafast laser beams [36–38] offers a unique opportunity to explore novel possibilities in HHG. While the electric fields associated with multi-terawatt or -petawatt lasers are typically well above the ionization saturation limit and, therefore, useless for HHG, the associated magnetic fields are strong enough to introduce substantial modifications of the electronic dynamics leading to harmonic generation. A relevant scenario for B-field-assisted HHG is, therefore, the combination of ultraintense lasers together with the traditional infrared driving, in spatial regions where the ultraintense B-field can be found isolated from the associated E-field. There are several schemes that have proposed the generation of such intense B-fields, through the use of femtosecond relativistic interactions [39], plasma physics [40], or ultrafast azimuthally polarized vector beams [41–43]. An appealing scheme, considered in this article, consists in the use of 2 counter-propagating high-power laser beams, in which one can identify nodal regions in which the B-field amplitude dominates (see Fig. 1A).

In this article, we identify a novel regime in which HHG assisted by intense isolated B-fields leads to the generation of near Fourier-limited attosecond pulses. We propose to drive HHG in an atomic gas by a moderately intense circularly polarized laser beam, assisted by an intense B-field (see Fig. 1). In this scenario, the assisting B-field introduces a transverse trapping to the dynamics of the ionized electron, i.e., effectively forming a quantum wire (QW) [44]. This transverse confinement of the electron wavepacket introduces new characteristics to the HHG process. In the first place, it reduces the wavepacket lateral dispersion, enhancing the efficiency of the harmonic
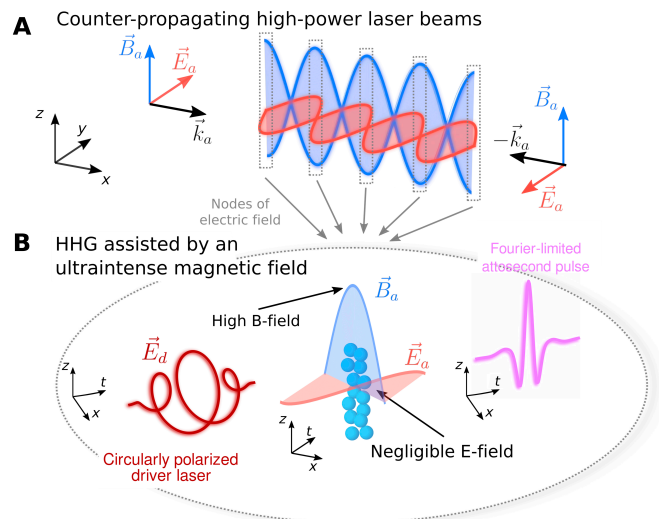

Fig. 1. Scheme of HHG assisted by an intense B-field to generate near Fourier-limit attosecond pulses. (A) The assisting B-field is obtained from the use of 2 counter-propagating high-power laser beams. At the nodes of the E-field, $\vec{E}_a$, the B-field, $\vec{B}_a$, reaches its maximum value (marked as gray boxes), and it can be considered as locally isolated from the E-field. (B) The proposed HHG scheme is driven by a moderately intense circularly polarized (CP) laser, $\vec{E}_d$, oscillating in the x–z plane and propagating in the y direction, assisted by the intense linearly polarized B-field, $\vec{B}_a$, oscillating in the z direction. The far-field harmonic emission detected along the y direction, composed of near Fourier-limited attosecond pulses, is dominated by the dipole radiation created at the $\vec{E}_a$ nodes.

emission. In addition, it allows to populate high-energy vibrational states in the transverse coordinate, forced by the circularly polarized driving E-field, that serve as an energy reservoir to be released in the form of ultrahigh-frequency harmonic emission upon the rescattering of the electron with the parent ion. Finally, the lateral confinement restructures the electron density of states in the continuum into a set of discretized, equally spaced maxima, introducing a lateral breathing dynamics in the electron wavepacket. We shall see that a proper control of these characteristics allows for the emission of almost Fourier-limited soft x-ray isolated few-cycle attosecond pulses. We remark that, while challenging, the scenario of B-field-assisted HHG is feasible with the state-of-the-art multi-terawatt/petawatt laser sources and the current strategies for B-field isolation using structured fields, or simple standing-wave geometries. In return, we foresee a breakthrough scenario in HHG assisted by structured petawatt laser beams, where chirp-free x-ray high-order harmonics can be obtained, opening the route toward Fourier-limited few-*as* pulses. We remark that while in this article we consider the nodes of an ultraintense counter-propagating laser as a possibility for finding spatial regions with isolated B-fields, other possibilities to induce intense magnetic fields [39–42], or alternative schemes in which a transient QW structure for the detached electrons is created, could provide similar results.

Materials and Methods

The combined driving laser field—circularly polarized E-field assisted by a linearly polarized B-field—is sketched in Fig. 1. First, we consider a moderately intense (peak intensity of 1.6×10^{14} W/cm^2) circularly polarized driving field, $\vec{E}_d(t)$, oscillating at 0.8 µm wavelength in the x–z plane, and propagating

in the y direction. Note that the corresponding B-field, $\vec{B}_d(t)$—oscillating in the x–z plane—has a negligible effect in the electronic dynamics in our HHG configuration. Thus, the driving force is exerted mainly by the E-field and is given by

$$\vec{E}_d(t) = E_0 f(t) e^{i\omega_{0d}t}\left[\vec{u}_x + i\vec{u}_z\right] + c.c. \quad (1)$$

where E_0 is the E-field amplitude, ω_{0d} is its central frequency, and $f(t) = \sin^2\left(\pi\frac{t}{\tau_{max}}\right)$ is the temporal envelope function for $0 \le t \le \tau_{max}$, with $\tau_{max} = 3/8\tau_p$ being the total pulse duration. In the following results, τ_{max} is 10.5 fs for the the driving E-field and the assisting B-field. Note that the circularly polarized state of a driving E-field is known to prevent the appearance of high-order harmonics [45] in the traditional scheme. However, here we propose to assist the process by an intense (2.8×10^4 T) linearly polarized B-field, oscillating at 187 THz in the z direction. Such B-field is found almost isolated at the E-field nodes of 2 linearly polarized counter-propagating intense (peak intensity of 2.4×10^{18} W/cm²) laser beams, propagating in the $\pm x$ direction, and oscillating at λ_a=1.6µm wavelength.

Thus, the assisting B-field, $\vec{B}_a(t)$, can be described as

$$\vec{B}_a(t) = B_0 f(t) e^{i\left(\omega_{0a}t + \phi_a\right)}\vec{u}_z + c.c. \quad (2)$$

where E_0 is the B-field amplitude, ω_{0a} is the central frequency, and ϕ_a reflects the phase difference between $\vec{E}_d$ and $\vec{B}_a$. Importantly, note that the harmonic emission is directed perpendicular to the plane defined by the local field polarization $\vec{E}_a(t) + \vec{E}_d(t)$ and the gas jet. On the one hand, high harmonics generated at the assisting E-field nodes will propagate preferentially in the same direction as the driving field, i.e., the y axis. On the other hand, harmonic radiation generated at locations where the assisting E-field dominates the driving will be directed preferably along the z axis. Therefore, the HHG signal produced at the nodes of the assisting E-field, which are the relevant for this study, can be separated spatially from other contributions. From now on, we will concentrate on the study of the far-field harmonic emission detected along the y axis, dominated by HHG driven by $\vec{E}_d$ assisted by the isolated $\vec{B}_a$.

For simplicity, we test our ideas taking atomic hydrogen as target, though our conclusions could be extended to other noble gases. We consider a full 3-dimensional (3D) model for the hydrogen atom interacting with both fields, $\vec{E}_d$ and $\vec{B}_a$, governed by the Time-Dependent Schrödinger Equation (TDSE) $i\hbar\partial_t\Psi(\vec{r},t) = \hat{H}(\vec{r},t)\Psi(\vec{r},t)$. The Hamiltonian for the electronic wavefunction, $\Psi(\vec{r},t)$, in a uniform magnetic field polarized along the z axis [34,46] reads as:

$$\hat{H}_0 = \frac{\vec{p}^2}{2m_e} + \frac{q^2}{8m_e c^2}B_a^2(t)\left(x^2 + y^2\right) - \frac{q}{2m_e c}B(t)\hat{L}_z - \frac{q}{r} \quad (3)$$

where $\hat{L}_z$ is the orbital angular momentum operator along the z direction, parallel to $\vec{B}_a$. Now, we add the interaction with the external driving E-field $\vec{E}_d$ using the associated vector potential $\vec{A}_d = -c\int_\infty^t dt'\vec{E}_d(t')$, resulting in the following Hamiltonian:

$$\hat{H}_0 = \frac{1}{2m_e}\left[\vec{p} - \frac{q}{c}\vec{A}_d(t)\right]^2 + \frac{q^2}{8m_e c^2}B_a^2(t)\left(x^2 + y^2\right) - \frac{q}{2m_e c}B(t)\hat{L}_z - \frac{q}{r} \quad (4)$$

The TDSE is solved using a finite differences scheme for the spatial derivatives, while the temporal evolution is carried using the Crank-Nicolson algorithm. We consider the hydrogen ground state as the initial wavefunction, obtained via imaginary time propagation. The simulations are carried using a 0.12–Å spatial and 0.75 as temporal resolution. The box size used is $12 \times 12 \times 12$ nm.

In order to give insight into the physics beyond HHG assisted by an intense, ultrafast B-field, we have developed a simplified model to explore the transverse dynamics of the ionized electron. For this, we consider the electron released in the continuum at a particular ionization time, t_i, with a wavefunction with the same transverse profile as that the atomic ground state. Following the philosophy of the Strong-Field Approximation [47–49], once ionized, the electron is considered free from the interaction with the parent atom. Thus, our model Hamiltonian for the ionized electron has the same form as that in Eq. 4, but neglecting the Coulomb term. In doing so, the Hamiltonian becomes separable in cartesian coordinates. The main ideas from our model can be drawn focusing into the transverse x component, as it contains the excitations triggered by both the assisting B-field and the x-component of the driving E-field. Indeed, the dynamics in the longitudinal z coordinate corresponds to a quivering free electron, resulting from the interaction with the z component of the driving E-field. This can be understood semiclassically in terms of electron returning trajectories along the z axis. On the other hand, dynamics in the y direction is that of a parametric harmonic oscillator that induces low/medium energy excitations, therefore not relevant for ultrahigh HHG we are reporting in this study. Taking these considerations into account, we restrict our model to the solution of the 1D TDSE, for the free electron along the x coordinate under the Hamiltonian:

$$\hat{H}_{1D} = \frac{1}{2m_e}\left[p_x - \frac{q}{c}A_{d,x}\left(t + t_i\right)\right]^2 + \frac{1}{2}\Omega^2\left(t + t_i\right)x^2, \quad (5)$$

which describes transverse dynamics along the x axis as that of a free electron evolving under the influence of the x component of the driving field, and confined transversely by a parametric harmonic oscillator, whose time-dependent frequency is given by $\Omega(t) = \Omega_0\sqrt{1 - \cos\left(2\omega_{0a}t + 2\phi_a\right)}$ with $\Omega_0 = qB_0/2\sqrt{2}m_e c$. Note that the Hamiltonian in Eq. 5 can be factorized into a transversal harmonic oscillator with frequency Ω_0 plus an also harmonic, transverse time-dependent interaction: $\hat{H}_{1D} = \hat{H}_{ho} + \hat{V}_{int}(t)$, with $\hat{V}_{int}(t) = \frac{1}{2}\Omega_0^2\cos\left(2\omega_{0a}t + 2\phi_a\right)x^2$. The time evolution for the simplified model is solved using the Crank-Nicolson scheme in one dimension, and the spatial second derivatives are implemented using a finite difference method. The initial state in this case is assumed to have the same spatial profile as the hydrogen ground state, i.e., a decaying exponential $\sim e^{-x/a_0}$ where a_0 is the Bohr radius. The spatial resolution for this simplified model is increased up to 0.02 Å as the computational requirements are less demanding than in the complete 3D calculations.

Results and Discussion

In this section, we first show our main results from the full 3D simulations, which demonstrate the generation of chirp-free, Fourier-limited attosecond pulses. In the Transverse wavepacket dynamics section, we model the transverse dynamics of

the ionized electron using Eq. 5. With this simplified model, we successfully explain the underlying physics of the chirp-free emission, which is corroborated through the analysis of the HHG spectrograms of our full 3D simulations. Finally, we explore the HHG spectra dependency with the assisting B-field amplitude and the relative phase between the driving E-field and the assisting B-field in the HHG dependency on the assisting B-field amplitude and phase section.

Emission of chirp-free attosecond pulses

In Fig. 2A we present the resulting HHG spectrum of the full TDSE calculation, i.e., ruled by the Hamiltonian in Eq. 4 (orange line, $E_0 = 1.6 \times 10^{14}$ W/cm^2, $B_0 = 2.8 \times 10^4$ T). We compare it with the HHG emission obtained from a linearly polarized driving E-field without the external B-field (blue line, same E_0), which we will refer in the following as the standard HHG geometry.

Within the 3-step model, the cutoff energy for the standard geometry can be estimated by the well-known $\hbar\omega_{cutoff} \approx I_p + 3.17U_p$ law [15], where I_p is the ionization potential of the target and U_p corresponds to the ponderomotive energy of the driving field. In the case presented in Fig. 2, the maximum photon energy is $E_{cutoff} = 43$ eV (27th harmonic order). It is important to remark that if the driving E-field is circularly polarized, HHG emission is not possible in the absence of an external B-field due to the highly inefficient recollision between the detached electrons and the parent ions [45]. Remarkably, if the circularly polarized driving E-field is assisted by an intense isolated B-field (orange line in Fig. 2A), not only HHG is efficient, but the harmonic spectrum shows a second, broader, plateau that extends to the 200th harmonic order (4 nm, 310 eV).

Here, it is important to remark that the primary cutoff could be extended already with intense E-fields like those associated with the assisting B-field we are considering. However, one of the most striking properties of this second plateau, beyond its broadness, is the absence of attochirp. Figure 2B presents the temporal HHG emission after filtering out harmonics below the 70th (orange line), reaching $\tau_{FWHM} = 27$ as. Noticeably, the corresponding Fourier-limited pulse (green) presents $\tau_{FWHM, FL} = 21$ as, which evidences that the second plateau is composed

of chirp-free high-order harmonics. In addition, the as pulse is almost single cycle (the temporal period of the the central wavelength, 6.7 nm, is 22 as). The Fourier limit is obtained after taking the complex orange spectrum in Fig. 2A and considering a flat phase profile. Then, the Fourier transform of this modified spectrum yields the Fourier-limited attosecond pulse emission.

Transverse wavepacket dynamics

In order to understand the physics beyond the chirp-free harmonic emission, we resort to the scattering model already introduced in the Materials and Methods section. In Fig. 3A, we present the eigenstates of the Hamiltonian, Eq. 3, composed only by the atomic and the parabolic potential created at the assisting B-field maximum, without the interaction with the driving E-field. The B-field harmonic trapping structures the continuum eigenstates. The density of states (DOS), number of allowed states per energy range, for unbounded states is modulated into a series of peaks located around multiples of Ω_0, the energy levels of the B-field induced harmonic trap, as shown in Fig. 3B. The resulting DOS clearly shows how the assisting B-field acts as a confining potential inducing a continuum restructuring of the states similar to QW, a nanostructure with 2 confined dimensions, whose DOS is plotted with the solid oranges line in Fig. 3B [50].

Beyond the trapping potential from the mean B-field component, its oscillatory behavior excites the low-lying states of the B-field harmonic oscillator. With a linearly polarized driving E-field, parallel to $\vec{B}_a(t)$, the transverse dynamics result only from the B-field oscillation, limiting the number of harmonic oscillator excited states. The use of a circularly polarized driving E-field forces the transverse harmonic oscillator promoting the ionized electronic wavepacket to extremely high excited states, with a vast energy-level span. The large number of excited states in a harmonic oscillator results in a semiclassical wavepacket analogous to a squeezed coherent state [51]. During the recollision, this high-energy excitation translates to an extended HHG spectrum, well beyond that obtained with a linearly polarized driving E-field.
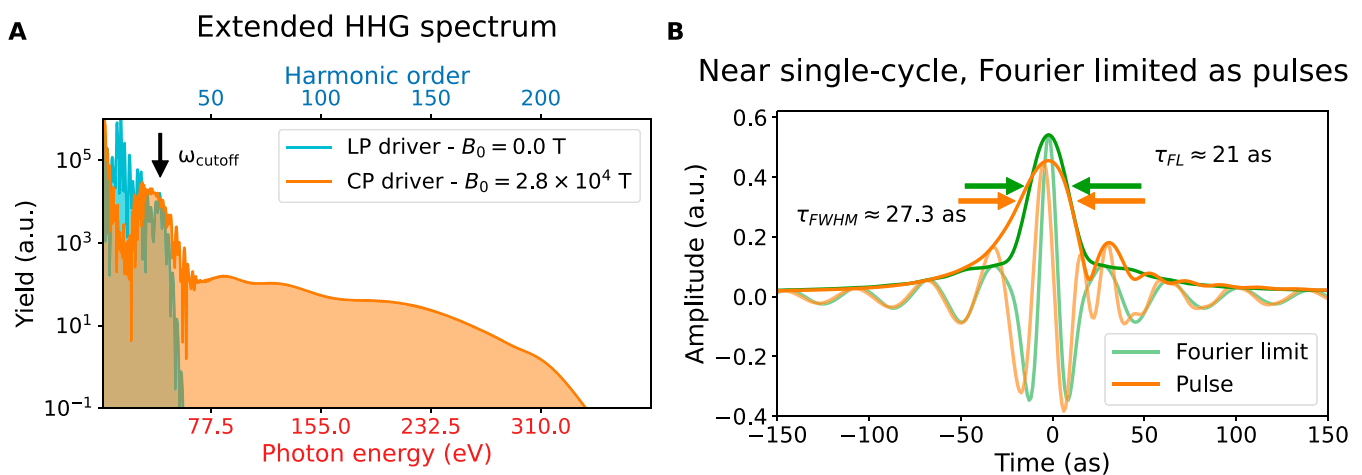
A

Extended HHG spectrum

B

Near single-cycle, Fourier limited as pulses

Fig. 2. (A) HHG spectrum comparison between the standard scheme (blue line)—linearly polarized (LP) driver E-field without the assisting B-field—and the proposed scheme (orange line), with an assisting B-field of amplitude 2.8×10^4 T. The black arrow points out the classical cutoff energy 43 eV given by the 3-step model. (B) Attosecond pulse obtained by filtering out the HHG emission below 108 eV for the orange spectrum shown in (A). The pulse exhibits a 27-as FWHM duration, close to the 21-as Fourier limit. The pulse is centered at 6.7-nm wavelength (185 eV).
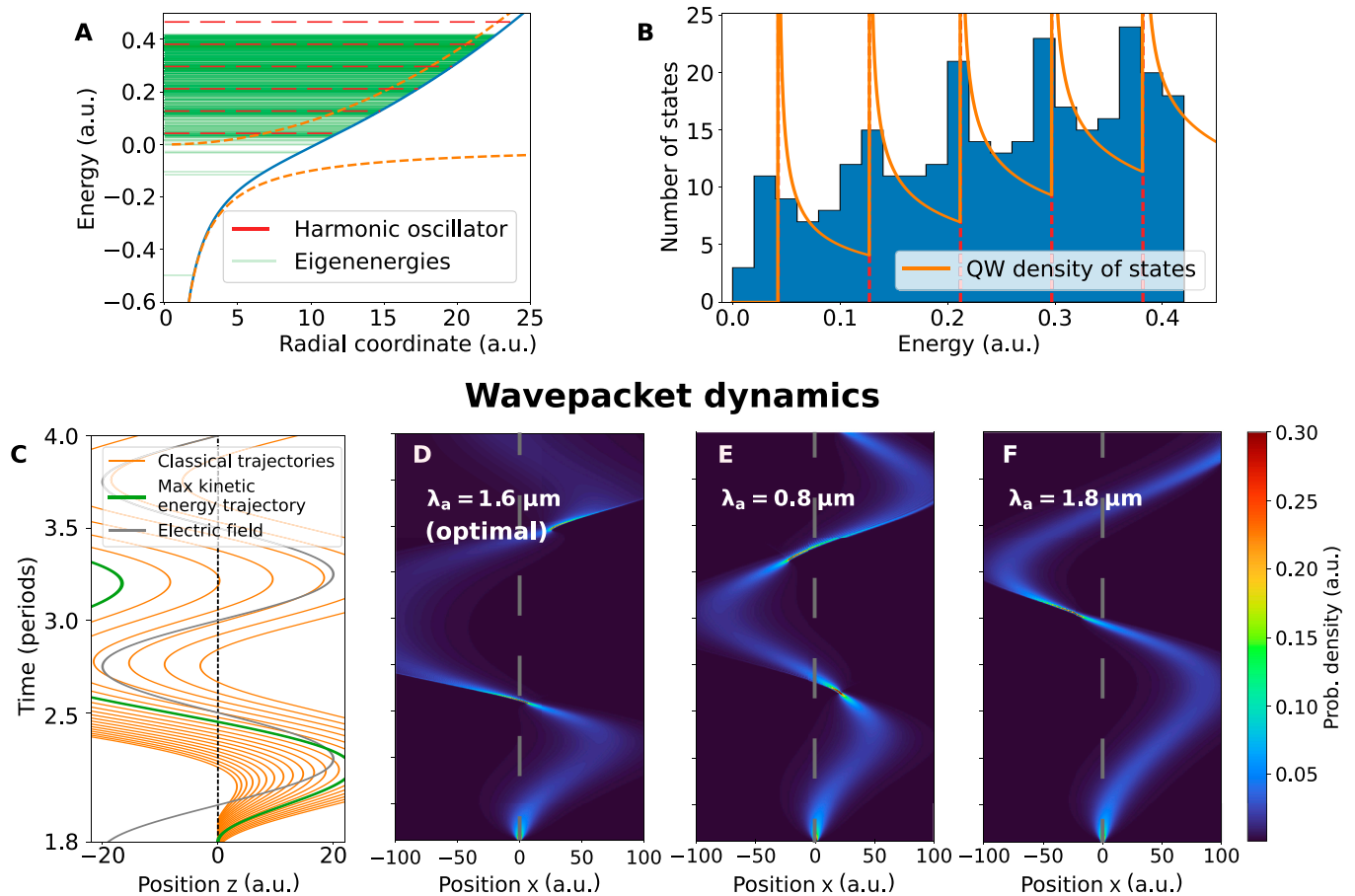
Wavepacket dynamics

Fig. 3. (A) Eigenenergies (green lines) obtained via diagonalization of the Hamiltonian composed by the assisting B-field harmonic oscillator and the atomic potential (dashed orange lines), along the eigenenergies for the harmonic oscillator $\widehat{H}_{ho}$ (dashed red lines) $E_n = \Omega_0 \left(n + \frac{1}{2} \right)$. (B) Number of states distribution in the electron continuum (blue bars). The distribution follows the density of states of a QW structure (orange line). The density of states (DOS) for the QW is given by $\mathrm{DOS}(E) = \left(\frac{E - E_n}{2} \right)^{-1/2}$. (C) Longitudinal classical trajectories for the electron ionized at different times (orange lines). The most energetic trajectory at the ion rescattering is plotted in green. The gray line shows the longitudinal component of the driving E-field. (D) Wavepacket evolution in the transverse direction given by our 1D model, proposed in Eq. 5, under the action of the assisting B-field harmonic oscillator, with $\lambda_a = 1.6\,\mu m$, and the driving E-field along the x direction. The wavepacket is assumed to be ionized at $t_i = 1.8$ periods. The effect of the atomic potential is disregarded in this approximation. The focusing event happens almost at the same time as the recollision in the longitudinal oscillation direction, shown in panel (C). Panels (E) and (F) show similar results as in panel (D), but with $\lambda_a = 0.8\,\mu m$ and $\lambda_a = 1.8\,\mu m$, respectively. In these latter cases, the transversal wavefunction compression does not coincide with the parent ion position (dashed gray line), and thus the harmonic emission and maximum photon energy are substantially reduced.

In order to illustrate the wavepacket dynamics, we show in Fig. 3C and D its longitudinal and transverse temporal evolution. In the longitudinal direction (Fig. 3C), the relevant dynamics is that of the mean wavepacket position and, therefore, it can be described using a classical trajectory for each ionization time. The trajectory that leads to the maximum kinetic energy at recollision is represented in green. In Fig. 3D we show the transverse dynamics evolution obtained from our model. The mean position of the wavepacket follows a semiclassical trajectory, and the transverse magnetically controlled spread of the wavepacket results into a breathing mode that leads to a series of attosecond transient focusing. We can see how the focusing event of the wavepacket's transverse component temporally coincides with the recollision event given by the classical quivering dynamics in the longitudinal direction, leading to the high-energy, chirp-free attosecond pulse.

If the assisting B-field parameters are properly chosen, the transversal focusing of the wavefunction can be sychronized with an electron rescattering event, thus maximizing the efficiency of the harmonic generation at selected times. Figure 3D, where

$\lambda_a = 1.6\,\mu m$, shows an example of this parameter choice. We show in Fig. 3E and F the resulting wavepacket dynamics when using $\lambda_a = 0.8\,\mu m$ and $\lambda_a = 1.8\,\mu m$, respectively. In these latter cases, the time of maximum transverse compression of the wavefunction is shifted, and both the harmonic emission and the maximum photon energy are substantially weaker (not shown). The effective rescattering and focusing events synchronization will depend not only on the field frequencies as already shown, but also on the phase and strength of the assisting B-field, as depicted hereunder.

Our conclusions from the one-dimensional model are corroborated when looking at the time–frequency analysis of the full-calculation spectra shown in Fig. 2A. In Fig. 4 we show the spectrogram (also denoted as time–frequency analysis) of the harmonic emission obtained from (a) the linearly polarized driver E-field without the B-field, $\vec{B}_a = 0$, and (b) the circularly polarized driver E-field assisted by the B-field, $\vec{B}_a$. In the first case, the well-known short (long) trajectory contributions are clearly identified with the positive (negative) slope time–frequency structures, which reflect the presence of the positive

(negative) attochirp [16,17,52]. However, the interplay of the circularly polarized driver field with the B-field results in a flat—no slope—time–frequency structure, indicating a chirp-free harmonic emission. According to our interpretation, the absence of attochirp originates from the almost instantaneous increase of the HHG efficiency associated with the transverse wavefunction compression during the breathing cycle. In Fig. 4C and D the corresponding attosecond pulses are shown (orange lines), together with their Fourier-limited emission (blue lines), reflecting how the assisting B-field reduces the chirp of the attosecond emission.

The time–frequency analysis in Fig. 4B shows the emission of an isolated attosecond pulse. This temporal isolated emission arises as only one maximum compression event is synchronized with HHG recollision through the interaction time. In other words, the generation of an isolated attosecond pulse is linked with the transverse harmonic dynamics introduced by the assisting B-field. As such, the cadence of the attosecond pulse production is half cycle of the assisting B-field. In the case depicted in Fig. 4B and D, the driving E-field and assisting B-field wavelengths of 0.8 μm and 1.6 μm, respectively, dictate the production of 1-*as* pulse every full period of the driving E-field. The short duration of the driving E-field pulse (3.6 fs full width at half maximum in intensity) restricts the emission to a single isolated attosecond pulse. Note that longer driving

E-field and assisting B-field pulses result in a train of chirp-free attosecond pulses.

HHG dependency on the assisting B-field amplitude and phase

Finally, we present how the magnetically assisted HHG spectrum depends on the assisting B-field amplitude, B_0, and phase, ϕ_a. On the one hand, in Fig. 5A, we present a scan of the HHG spectra where B_0 is varied from 0 to 12×10^4 T, with a laser peak intensity of $E_0^2 = 1.6 \times 10^{14}$ W/cm^2 and the same phase between both fields, $\phi_a = 0$. Interestingly, the spectrum enhancement is stronger for 2.5×10^4 T $\le B_0 \le 5 \times 10^4$ T and $B_0 \ge 6.4 \times 10^4$ T, giving the broadest HHG spectrum at 2.8×10^4 T (which corresponds to that presented in Figs. 2 and 4B). The HHG spectra dependency with the assisting B-field amplitude can be explained by inspecting the lateral wavepacket dynamics given by the one-dimensional model. In Fig. 5B we present the transverse wavepacket dynamics for different values of the assisting B-field amplitude, lower and higher than the optimum value ($B_0 = 2.8 \times 10^4$ T). For the cases presented, neither the focusing nor the ion crossing are temporally synchronized and/or spatially overlapped with the longitudinal recollision event, shown in Fig. 3C. Only for $B_0 = 2.8 \times 10^4$ T (Fig. 3D) do the maximum wavepacket compression and the recollision in the longitudinal quivering trajectories take place together, maximizing the emission and broadening the spectrum.
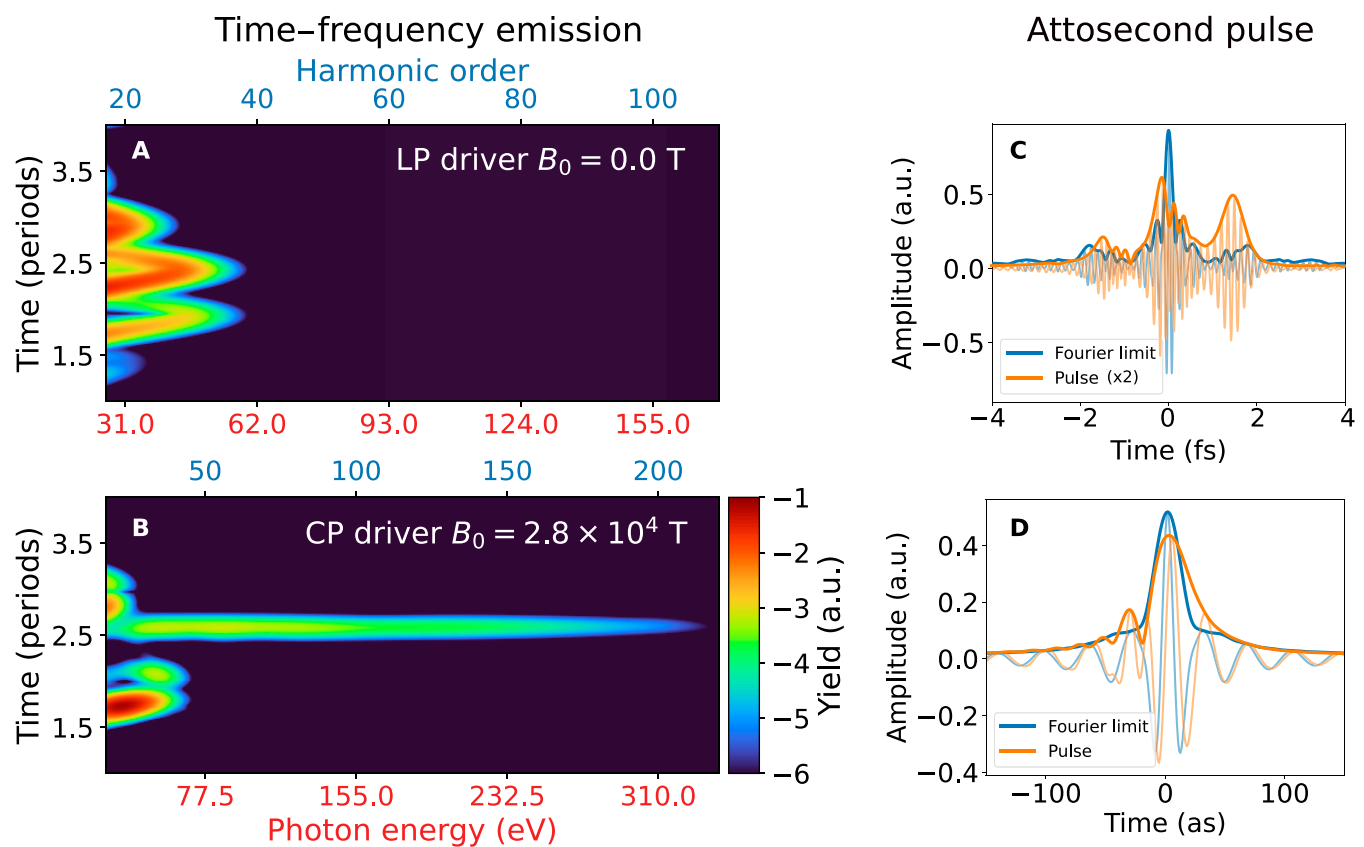
Fig. 4. Time–frequency comparison between the standard HHG scheme (A)—with a linearly polarized driving E-field and no assisting B-field—and the magnetically assisted HHG scheme (B)—with the circularly polarized driving E-field and linearly polarized assisting B-field. In the former case, there is a clear chirped emission reflecting the short (positive slope) and long (negative slope) trajectory contributions. In the latter case, the emission results in a flat, chirp-free, structure. These time–frequency analyses are obtained from the spectra shown in Fig. 2A. Panels (C) (linearly polarized driving E-field without assisting B-field) and (D) (circularly polarized driving E-field with the assisting B-field) show the corresponding attosecond pulse emission by filtering harmonic orders below the 20th order and 70th order, respectively. In both cases, the attosecond pulse is plotted in orange, whereas the Fourier-limited pulse is in blue.
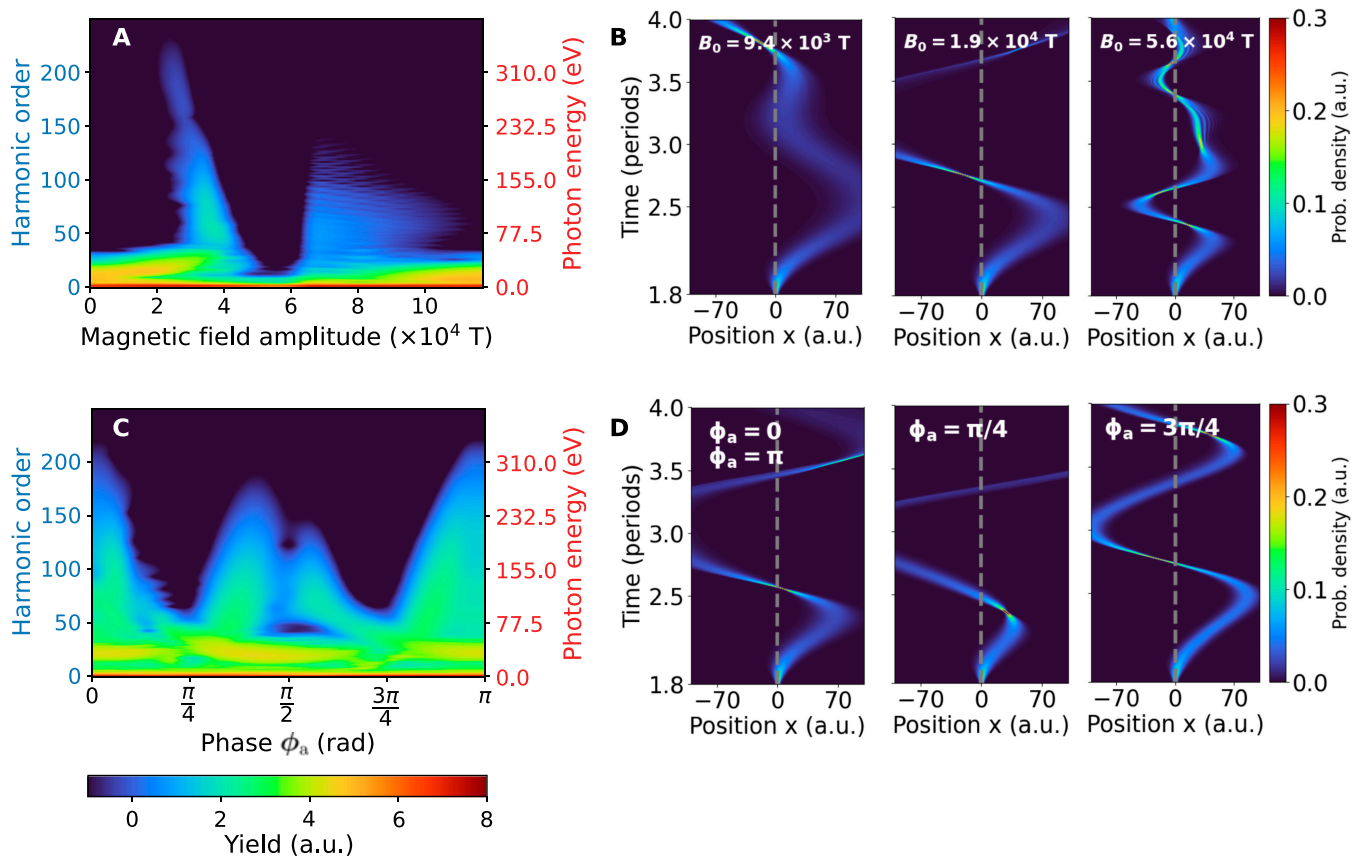
Fig. 5. (A) HHG spectrum as a function of the assisting B-field amplitude, ranging from 0 to 12×10^4 T ($\phi_a = 0.0$). The broadest spectrum is obtained for an assisting B-field amplitude of $B_0 = 2.8\times10^4$ T. (B) Transversal wavepacket dynamics calculated using the one-dimensional model presented in Eq. 5 The driving E-field and the assisting B-field are oscillating on phase. (C) HHG spectrum as a function of the relative phase between the driving E-field and the assisting B-field, ϕ_a (where $B_0 = 2.8\times10^4$ T). The scan shows a reduction of the spectrum width for $\phi_a = \pi/4$ and $\phi_a = 3\pi/4$. This dependency is π-periodic. The driving E-field has the same parameters as in Fig. 2. (D) Lateral wavepacket dynamics for different relative phases ϕ_a. The assisting B-field amplitude is $B_0 = 2.8\times10^4$ T. All the calculations are performed using a $1.6-\mu$m B-field wavelength and a 10.5-fs pulse duration

On the other hand, in Fig. 5C, we show the HHG spectrum dependency on the phase ϕ_a between the driving E-field and assisting B-field, for $B_0 = 2.8 \times 10^4$ T, and the same E-field used previously. The spectrum depends not only on the B-field amplitude, but also on the relative phase, so the broad plateau is strongly damped for phases $\phi_a = n\pi/4$, with n odd integer. Relative phase variations between the driving E-field and the assisting B-field will result in displacements of the maximum compression event, as depicted in Fig. 5D. Only for $\phi_a = n\pi/4$ does the wavepacket maximum compression coincide with the recollision event, and it is spatially overlapped with the ion position, leading to the maximum process efficiency. For any other values of ϕ_a, there is a lack of temporal synchronization and/or spatial overlapping, resulting in an inefficient process and therefore the damped plateau.

A precise selection of the assisting B-field parameters is thus required to maximize the efficiency and broadness of the HHG spectrum. This fact is relevant for macroscopic phase-matching, as it means that only certain regularly spaced regions in the target would contribute efficiently to the second plateau emission. As such, the generation of chirped-free attosecond pulses is preserved in the macroscopic picture.

Conclusion

In conclusion, we introduce an HHG scheme where the interplay of a circularly polarized E-field driver and an intense, ultrafast

linearly polarized B-field results in the generation of broad chirp-free high-order harmonic radiation. The chirp-free emission allows the generation of almost Fourier-limited few-cycle attosecond pulses. We have developed a simple physical model that shows how the B-field can be used to induce and control a transverse electron breathing wavepacket dynamics, by restructuring the continuum into a form analogous to a QW trapping.

Our proposal reveals a new scenario where intense, multiterawatt or -petawatt class lasers are used to assist HHG by modifying the electron continuum structure. We demonstrate the possibility of producing soft x-ray few-cycle isolated attosecond pulses near the Fourier limit.

This is particularly interesting in the soft x-rays, where traditional chirp compensation devices are highly inefficient. With the use of driving E-fields with longer, mid-infrared wavelengths [14,53–56], we foresee a unique opportunity to generate extremely broad chirp-free HHG spectra, with potential to reach few-cycle few-*as*, or even sub-*as* pulses.

Acknowledgments

Data Availability

The data that support the findings of this study are available from the authors upon reasonable request.

References

1. Krausz F, Ivanov M. Attosecond physics. *Rev Mod Phys*. 2009;81:163.
2. Shi X, Liao C-T, Tao Z, Cating-Subramanian E, Murnane MM, Hernandez-García C, Kapteyn HC. Attosecond light science and its application for probing quantum materials. *J Phys B Atomic Mol Phys*. 2020;53(18):Article 184008.
3. Midorikawa K. Progress on table-top isolated attosecond light sources. *Nat Photonics*. 2022;16:267–278.
4. Hentschel M, Kienberger R, Spielmann C, Reider GA, Milosevic N, Brabec T, Corkum P, Heinzmann U, Drescher M, Krausz F. Attosecond metrology. *Nature*. 2001;414(6863):509–513.
5. Drescher M, Hentschel M, Kienberger R, Uiberacker M, Yakovlev V, Scrinzi A, Westerwalbesloh T, Kleineberg U, Heinzmann U, Krausz F. Time-resolved atomic inner-shell spectroscopy. *Nature*. 2002;419(6909):803–807.
6. Wörner HJ, Arrell CA, Banerji N, Cannizzo A, Chergui M, Das AK, Hamm P, Keller U, Kraus PM, Liberatore E, et al. Charge migration and charge transfer in molecular systems. *Struct Dyn*. 2017;4(6):Article 061508.
7. Calegari F, Trabattoni A, Palacios A, Ayuso D, Castrovilli MC, Greenwood JB, Decleva P, Martín F, Nisoli M. Charge migration induced by attosecond pulses in bio-relevant molecules. *J Phys B Atomic Mol Phys*. 2016;49(14):Article 142001.
8. Wielopolski M, Marszalek M, Brunetti FG, Joly D, Calbo J, Aragó J, Moser J-E, Humphry-Baker R, Zakeeruddin SM, Luis J, et al. Synthesis and optoelectronic properties of chemically modified bi-fluorenylidenes. *J Mater Chem C*. 2016;4:3798–3808.
9. Smolentsev G, Cecconi B, Guda A, Chavarot-Kerlidou M, van Bokhoven JA, Nachtegaal M, Artero V. Microsecond x-ray absorption spectroscopy identification of CoI intermediates in cobaloxime-catalyzed hydrogen evolution. *Chem Eur J*. 2015;21(43):15158–15162.
10. Duris J, Li S, Driver T, Champenois EG, MacArthur JP, Lutman AA, Zhang Z, Rosenberger P, Aldrich JW, Coffee R, et al. Tunable isolated attosecond X-ray pulses with gigawatt peak power from a free-electron laser. *Nat Photonics*. 2020;14(1):30–36.
11. Driver T, Li S, Champenois EG, Duris J, Ratner D, Lane TJ, Rosenberger P, AlHaddad A, Averbukh V, Barnard T, et al. Attosecond transient absorption spooktroscopy: A ghost imaging approach to ultrafast absorption spectroscopy. *Phys Chem Chem Phys*. 2020;22(5):2704–2712.
12. Paul PM, Toma ES, Breger P, Mullot G, Augé F, Balcou P, Muller HG, Agostini P. Observation of a train of attosecond pulses from high harmonic generation. *Science*. 2001;292(5522):1689–1692.
13. Schafer KJ, Yang B, DiMauro LF, Kulander KC. Above threshold ionization beyond the high harmonic cutoff. *Phys Rev Lett*. 1993;70(11):1599–1602.
14. Popmintchev T, Chen M-C, Popmintchev D, Arpin P, Brown S, Aliauskas S, Andriukaitis G, Balfciunas T, Mücke OD, Pugzlys A, et al. Bright coherent ultrahigh harmonics in the keV x-ray regime from mid-infrared femtosecond lasers. *Science*. 2012;336(6086):1287–1291.
15. Lewenstein M, Balcou P, Ivanov MY, L'Huillier A, Corkum PB. Theory of high-harmonic generation by low-frequency laser fields. *Phys Rev A*. 1994;49:2117–2132.
16. Mairesse Y, de Bohan A, Frasinski LJ, Merdji H, Dinu LC, Monchicourt P, Breger P, Kovačev M, Taïeb R, Carré B, et al. Attosecond synchronization of high-harmonic soft X-rays. *Science*. 2003;302(5650):1540–1543.
17. Varjú K, Mairesse Y, Carré B, Gaarde MB, Johnsson P, Kazamias S, López-Martens R, Mauritsson J, Schafer KJ, Balcou PH, et al. Frequency chirp of harmonic and attosecond pulses. *J Mod Opt*. 2005;52(2-3):379–394.
18. Gaarde MB, Tate JL, Schafer KJ. Macroscopic aspects of attosecond pulse generation. *J Phys B Atomic Mol Phys*. 2008;41:Article 132001.
19. López-Martens R, Varju K, Johnsson P, Mauritsson J, Mairesse Y, Salieres P, Gaarde MB, Schafer KJ, Persson A, Svanberg S, et al. Amplitude and phase control of attosecond light pulses. *Phys Rev Lett*. 2005;94:Article 033001.
20. Li J, Ren X, Yin Y, Zhao K, Chew A, Cheng Y, Cunningham E, Wang Y, Hu S, Wu Y, et al. 53-attosecond X-ray pulses reach the carbon K-edge. *Nat Commun*. 2017;8:Article 186.
21. Gaumnitz T, Jain A, Pertot Y, Huppert M, Jordan I, Ardana-Lamas F, Wörner HJ. Streaking of 43-attosecond soft-x-ray pulses generated by a passively cep-stable mid-infrared driver. *Opt Express*. 2017;25(22):27506–27518.
22. Takahashi EJ, Kanai T, Ishikawa KL, Nabekawa Y, Midorikawa K. Coherent water window x ray by phase-matched high-order harmonic generation in neutral media. *Phys Rev Lett*. 2008;101:Article 253901.
23. Johnson AS, Austin DR, Wood DA, Brahms C, Gregory A, Holzner KB, Jarosch S, Larsen EW, Parker S, Strber CS, et al. High-flux soft x-ray harmonic generation from ionization-shaped few-cycle laser pulses. *Sci Adv*. 2018;4(5):Article eaar3761.
24. Schötz J, Förg W, Schweinberger I, Liontos HA, Masood AM, Kamal C, Jakubeit NG, Kling T, Paasch-Colberg SB, Biswas S, et al. Phase-matching for generation of isolated attosecond XUV and soft-x-ray pulses with few-cycle drivers. *Phys Rev X*. 2020;10:Article 041011.
25. Chipperfield LE, Robinson JS, Tisch JWG, Marangos JP. Ideal waveform to generate the maximum possible electron recollision energy for any given oscillation period. *Phys Rev Lett*. 2009;102:Article 063003.
26. Haessler S, Balčiunas T, Fan G, Andriukaitis G, Pugžlys A, Baltuška A, Witting T, Squibb R, Zaïr A, Tisch JWG, et al. Optimization of quantum trajectories driven by strong-field waveforms. *Phys Rev X*. 2014;4:Article 021028.

27 Fleischer A, Kfir O, Diskin T, Sidorenko P, Cohen O. Spin angular momentum and tunable polarization in high-harmonic generation. *Nat Publ Group*. 2014;8(7):543–549.

28 Fan T, Grychtol P, Knut R, Hernández-García C, Hickstein DD, Zusin D, Gentry C, Dollar FJ, Mancuso CA, Hogle CW, et al. Bright circularly polarized soft x-ray high harmonics for x-ray magnetic circular dichroism. *Proc Natl Acad Sci USA*. 2015;112(46):14206–14211.

29 Kim S, Jin J, Kim Y-J, Park I-Y, Kim Y, Kim S-W. High-harmonic generation by resonant plasmon field enhancement. *Nature*. 2008;453(7196):757–760.

30 Pérez-Hernández JA, Roso L, Zaïr A, Plaja L. Valley in the efficiency of the high-order harmonic yield at ultra-high laser intensities. *Opt Express*. 2011;19(20):19430–11439.

31 Odžak S, Milošević DB. Attosecond pulse generation by a coplanar circular and static field combination. *Phys Lett*. 2006;355(4-5):368–372.

32 Ludwig A, Maurer J, Mayer BW, Phillips CR, Gallmann L, Keller U. Breakdown of the dipole approximation in strong-field ionization. *Phys Rev Lett*. 2014;113:Article 243001.

33 Galloway BR, Popmintchev D, Pisanty E, Hickstein DD, Murnane MM, Kapteyn HC, Popmintchev T. Lorentz drift compensation in high harmonic generation in the soft and hard x-ray regions of the spectrum. *Opt Express*. 2016;24(19):21818–21832.

34 Milošević DB, Starace AF. High-order harmonic generation in magnetic and parallel magnetic and electric fields. *Phys Rev A*. 1999;60:3160–3173.

35 Milošević DB, Starace AF. Magnetic-field-induced intensity revivals in harmonic generation. *Phys Rev Lett*. 1999;82:2653–2656.

36 Leblanc A, Denoeud A, Chopineau L, Mennerat G, Martin P, Quéré F. Plasma holograms for ultrahigh-intensity optics. *Nat Phys*. 2017;13(5):440–443.

37 Longman A, Salgado C, Zeraouli G, Apiñaniz JI, Pérez-Hernández JA, Eltahlawy MK, Volpe L, Fedosejevs R. Off-axis spiral phase mirrors for generating high-intensity optical vortices. *Opt Lett*. 2020;45(8):2187–2190.

38 Döpp A. Plasma optics improving plasma accelerators. *Light Sci Appl*. 2022;11:Article 239.

39 Raj G, Kononenko O, Gilljohann MF, Doche A, Davoine X, Caizergues C, Chang Y-Y, Couperus Cabadağ JP, Debus A, Ding H, et al. Probing ultrafast magnetic-field generation by current filamentation instability in femtosecond relativistic laser-matter interactions. *Phys Rev Res*. 2020;2(2):Article 023123.

40 Shi Y, Vieira J, Trines RMGM, Bingham R, Shen BF, Kingham RJ. Magnetic field generation in plasma waves driven by copropagating intense twisted lasers. *Phys Rev Lett*. 2018;121:Article 145002.

41 Blanco M, Cambronero F, Flores-Arias MT, Conejero Jarque E, Plaja L, Hernández-García C. Ultraintense femtosecond magnetic nanoprobes induced by azimuthally polarized laser beams. *ACS Photonics*. 2019;6(1):38–42.

42 Sederberg S, Kong F, Hufnagel F, Zhang C, Karimi E, Corkum PB. Vectorized optoelectronic control and metrology in a semiconductor. *Nat Photonics*. 2020;14(11):680–685.

43 Jana K, Herperger KR, Kong F, Mi Y, Zhang C, Corkum PB, Sederberg S. Reconfigurable electronic circuits for magnetic fields controlled by structured light. *Nat Photonics*. 2021; 15(8):622–626.

44 Band YB, Avishai Y. 13—Low-dimensional quantum systems. In: Band YB, Avishai Y, editors. *Quantum mechanics with applications to nanotechnology and information science*. Amsterdam (Netherlands): Academic Press; 2010. p. 749–823.

45 Budil KS, Salières P, L'Huillier A, Ditmire T, Perry MD. Influence of ellipticity on harmonic generation. *Phys Rev A*. 1993;48:R3437–R3440.

46 Bransden BH, Joachain CJ. *Physics of atoms and molecules*. Pearson Education India; 2003.

47 Keldysh LV. Ionization in the field of a strong electromagnetic wave. *Zh Eksperim i Teor Fiz*. 1965;47(5):1945.

48 Faisal FHM. Multiple absorption of laser photons by atoms. *J Phys B Atom Mol Phys*. 1973;6(4):L89–L92.

49 Reiss HR. Effect of an intense electromagnetic field on a weakly bound system. *Phys Rev A*. 1980;22:1786–1813.

50 Mintmire JW, White CT. Universal density of states for carbon nanotubes. *Phys Rev Lett*. 1998;81:2506–2509.

51 Zhang W-M, Feng DH, Gilmore R. Coherent states: Theory and some applications. *Rev Mod Phys*. 1990;62:867.

52 Zair A, Holler M, Guandalini A, Schapper F, Biegert J, Gallmann L, Keller U, Wyatt AS, Monmayrant A, Walmsley IA, et al. Quantum path interferences in high-order harmonic generation. *Phys Rev Lett*. 2008;100:Article 143902.

53 Andriukaitis G, Balčiūnas T, Ališauskas S, Pugžlys A, Baltuška A, Popmintchev T, Chen M-C, Murnane MM, Kapteyn HC. 90 GW peak power few-cycle mid-infrared pulses from an optical parametric amplifier. *Opt Lett*. 2011;36(15):2755–2757.

54 Pupeza I, Sánchez D, Zhang J, Lilienfein N, Seidel M, Karpowicz N, Paasch-Colberg T, Znakovskaya I, Pescher M, Schweinberger W, et al. High-power sub-two-cycle mid-infrared pulses at 100 MHz repetition rate. *Nat Photonics*. 2015;9(11):721–724.

55 Vasilyev S, Moskalev IS, Smolski VO, Peppers JM, Mirov M, Muraviev AV, Zawilski K, Schunemann PG, Mirov SB, Vodopyanov KL, et al. Super-octave longwave mid-infrared coherent transients produced by optical rectification of few-cycle 2.5-μm pulses. *Optica*. 2019;6(1):111–114.

56 Elu U, Maidment L, Vamos L, Tani F, Novoa D, Frosz MH, Badikov V, Badikov D, Petrov V, St. J. Russell P, et al. Seven-octave high-brightness and carrier-envelope-phase-stable light source. *Nat Photonics*. 2021;15(4):277–280.